A Novel Method of Deep Tissue Biomedical Imaging Using a Wearable Sensor

Md Asiful Islam, *Student Member, IEEE,* Asimina Kiourti, *Member, IEEE,* John L. Volakis, *Fellow, IEEE*

***Abstract*— We present a novel monitoring method for continuous real-time imaging of deep human tissues using a body-worn sensor. The sensor operates at 40 MHz, and consists of a set of transmitting and receiving probes placed around the human body. For the first time, this portable and body-worn sensor provides for deep tissue pixel-by-pixel imaging. A demonstration of the concept is carried out by retrieving a 16-pixel image of the underlying cross-section with accuracy better than 6%. This paper also provides a theoretical analysis for assessing the sensor's accuracy. The analysis is based on line-source scattering by a 2-layer cylindrical model of the human torso. Full-wave simulations are then carried out to demonstrate the sensor's imaging capabilities pixel-by-pixel. Overall, the proposed sensor can be the basis for a portable and low-cost alternative to conventional imaging techniques suitable for a wide range of applications (among them, prevention of cardiovascular diseases and tumor growth monitoring).**

***Index Terms*—Biomedical sensor, human health monitoring, tissue dielectric properties, wearable electronics.**

I. Introduction

MAGNETIC Resonance Imaging (MRI), X-rays, Computed Tomography (CT) and Electrical Impedance Tomography (EIT) are the most popular surgery-free technologies used to image tissues deep into the human body [1]-[4]. However, these methods do not provide continuous real-time tissue characterization, as they are not portable systems. Also, these technologies are expensive, implying major access disparities. For continuous and low-cost monitoring of vital human body signals, several portable body-worn sensors have been reported [5]-[7]. Such sensors may pursue continuous monitoring of respiratory and heart rates, temperature or blood pressure. However, they do not include imaging capabilities. Therefore, there is a strong need to develop low-cost, portable devices for deep tissue imaging.

Recently, we proposed a body-worn sensor that can retrieve the average permittivity of deep human body tissues [8]-[10]. The sensor operated at 40 MHz, and consisted of a plurality of probes wrapped around the human body. Importantly, this sensor used a new algorithm for extracting the body's deep tissue permittivity. Specifically, the permittivity of the tissue's cross-section was determined by using a linear combination of the measured S-parameters from the receiving probes placed across the human body. As such, ill-posed matrices associated with classic inverse-scattering approaches [12]-[13] are avoided. Experimental results demonstrated that accuracy of this sensor is better than 11% [9]. Further, theoretical studies show that the sensor's accuracy can be increased to about 3% [10]. However, so far, the aforementioned studies treated the entire imaging domain below the skin, fat, muscle and bone as a bulk medium, having a single permittivity value, see Fig. 1a. That is, the sensor has yet to be adapted for pixel-by-pixel imaging of the body's cross-section as in Fig. 1b. Also, the theoretical studies in [10] considered a semi-infinite planar medium to model the human torso (see Fig. 1a), which was not realistic. That is, previous studies verified the concept and motivated more realistic imaging studies, as in this paper.

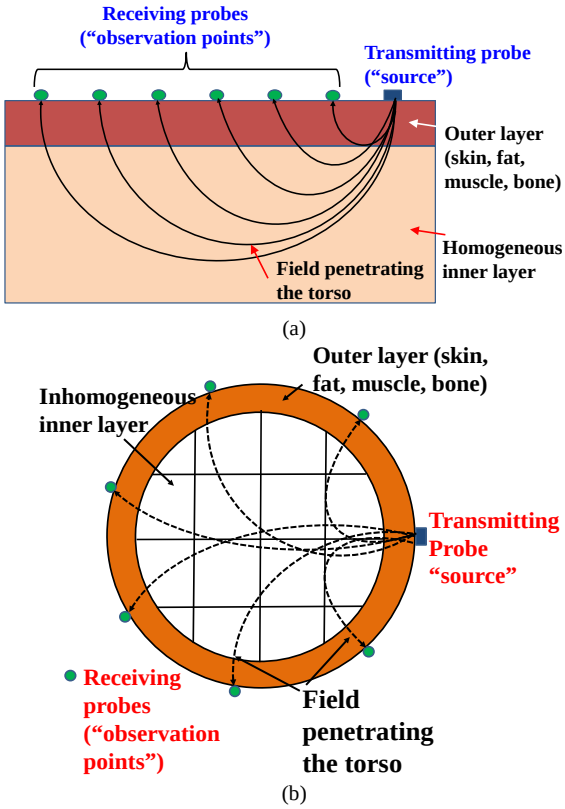

Fig. 1. (a) Previous studies, and (b) study in this paper.

Manuscript received July 31, 2015, revised September 04, 2015.

M.A. Islam, A. Kiourti and J.L. Volakis are with the ElectroScience Laboratory, Electrical and Computer Engineering Department, The Ohio State University, Columbus, OH 43212, USA (e-mail: islam.73@osu.edu, kiourti.1@osu.edu, volakis.1@osu.edu).

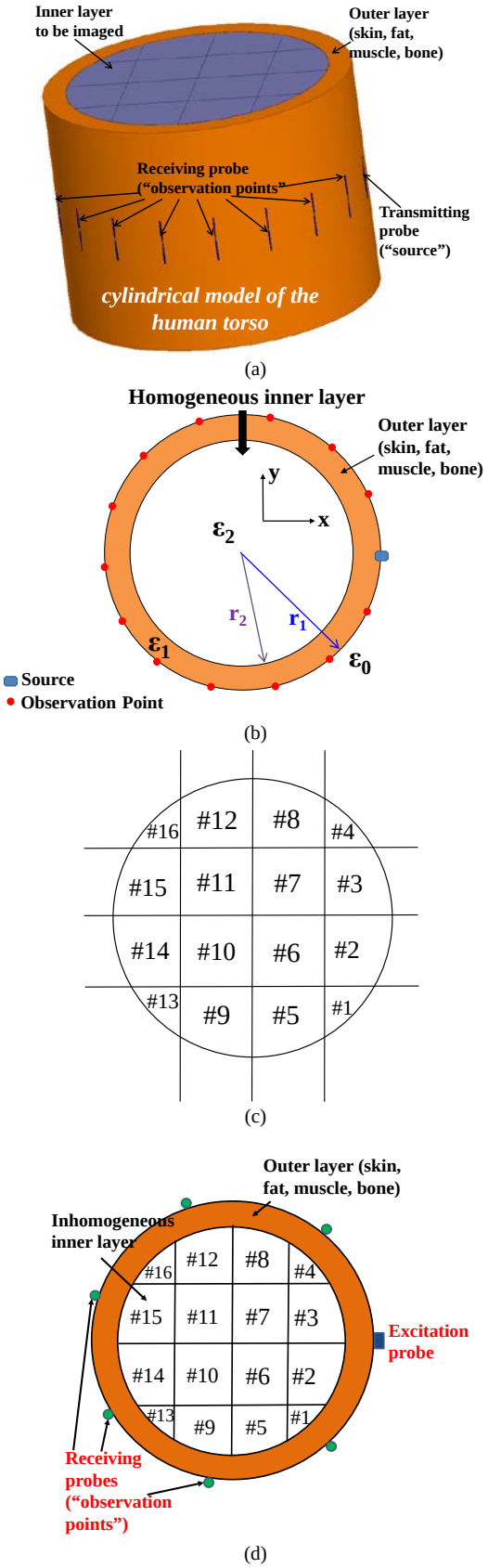

Fig. 2. (a) Proposed body-worn imaging sensor placed around a cylindrical model of the human torso, (b) cross-sectional view assuming homogeneous inner layer, (c) pixelization of the imaging domain using uniform square grid, and (d) cross-sectional view of the inhomogeneous torso after pixelization (# is the numbering from 1st to 16-th pixel).

In this work, we develop a body-worn monitoring method that images the permittivity and conductivity of the human torso's cross-section pixel-by-pixel. We believe that this is the first time that pixel-by-pixel permittivity and conductivity images of deep human tissues can be retrieved using a portable body-worn approach. Also, conductivity distribution of the underlying tissues is provided herewith for the first time.

The provided results demonstrate that the sensor can retrieve 16-pixel images of the human body with accuracy better than 6%. To our knowledge, this is the highest reconstruction accuracy reported for body-worn approaches used to image high-contrast inhomogeneous tissues deep into the body. The only requirement for the sensor operation relates to well-known estimates for: a) the torso circumference, and b) the average permittivity and conductivity of the imaging domain. The latter can be easily estimated using the method presented in [8], [9], [10]. Importantly, the proposed sensor can image any cross-section of the human body, for a very wide range of applications (e.g., prevention of cardiovascular diseases, tumor growth monitoring, detection of deep tissue injuries, etc.). Of importance is that this imaging method is not impacted by the skin, fat and muscle thickness.

This paper is organized as follows. Section II presents an overview of the sensor operation. Section III provides a theoretical analysis to assess the sensor's accuracy limits assuming a homogeneous cross-section. Section IV presents full-wave simulations to demonstrate the sensor's imaging capabilities.

II. Sensor Operation

As shown in Fig. 2a, the proposed sensor consists of a number of probes placed conformally around the body. One of the sensor probes is fed by a 40 MHz input signal ("source"), while the rest are used for receiving ("observation points").

The sensor can be placed around any portion of the human body to image the corresponding underlying cross-section. For validation, in this paper, the sensor is considered to be wrapped around a cylindrical model of the human torso. Specifically, the human torso will be modeled as a 2-layer cylinder, 18 cm in radius (see Fig. 2). For simplicity, the torso's skin, fat, muscle and bone tissues are combined into a single outer layer. That is, the properties of the outer layer are calculated by the weighted (in terms of thickness) average of skin, fat, muscle and bone tissues. Table I [10], [14]-[15] gives the aforementioned nominal values for these outer layers. Variations of the electrical properties and thicknesses of the outer layers are also provided in Table I. We clarify that the inner layer depicted in Fig. 2 represents the imaging domain. We also note that the input power at the "source" was 1 mW. As a result, the corresponding maximum Specific Absorption Rate averaged over 1g of tissue was $SAR1g,max \approx 0.2$ W/kg. This value is far below the limit 1.6 W/kg based on the IEEE C95.1-1999 [16] and FCC [17] safety exposure guidelines.

TABLE I
NOMINAL VALUES AND VARIATION RANGE OF TISSUE ELECTRICAL PROPERTIES AND THICKNESSES [10], [14] –[15]

Tissue	Permittivity (ε_r)	Loss tangent ($tan\delta$)	Thickness (h) [cm]
Skin	93.7±10%	2.17 ± 10%	0.3 ± 10%
Fat	7.33±10%	2.09 ± 10%	1.5 ± 10%
Muscle	82.6±10%	3.64 ± 10%	1.5 ± 10%
Bone	26±10%	1.55 ± 10%	2.0 ± 10%
Combination of skin, fat, muscle, bone	40.6±10%	2.33 ± 10%	5.3 ± 10%
Lung	65±40%	2.65 ± 20%	15 ± 20%

A. Homogeneous Inner Layer

As presented in [10], the electric fields at the probe observation points can be used to determine the average permittivity of the deeper human tissue. Specifically, the average permittivity of the inner cylindrical layer in Fig. 2b (imaging domain) can be expressed as:

$$\varepsilon_{r2} = \sum_{i=1}^{M} w_{\varepsilon,i} E_i \quad (1)$$

For this, M refers to the number of observation points, E_i is the electric field value at the i-th observation point, ε_{r2} is the relative permittivity of the homogeneous inner layer shown in Fig. 2b, and $w_{\varepsilon,i}$ are the unknown weight coefficients to be determined. This is done via a least-square method solution for a set of equations that enforce (1) for given ε_{r2} and E_i values.

A similar expression can also be introduced for the average conductivity of the inner cylindrical layer (imaging domain). Specifically, we have:

$$\sigma_2 = \sum_{i=1}^{M} w_{\sigma,i} E_i \quad (2)$$

where σ_2 is the conductivity of the homogeneous inner layer in Fig. 2b and $w_{\sigma,i}$ are the unknown weight coefficients to be found in a similar manner as $w_{\varepsilon,i}$.

As noted, the weight coefficients $w_{\varepsilon,i}$ and $w_{\sigma,i}$ can be calculated by enforcing (1) and (2) for a number of known ε_{r2} and σ_2 values. Concurrently, the permittivity, ε_r, loss tangent, $tan\delta$, and thickness, h, of the outer and inner tissue layers (see Table I) are varied. For N different combinations of outer tissues, we get the equations:

$$[\varepsilon_r]_{1\times N} = [w_\varepsilon]_{1\times M}[E]_{M\times N} \quad (3)$$
$$[\sigma]_{1\times N} = [w_\sigma]_{1\times M}[E]_{M\times N} \quad (4)$$

to be solved for $[w_\varepsilon]$ and $[w_\sigma]$ via the least squares method. This step can be referred to as the "training phase". Once $[w_\varepsilon]$ and $[w_\sigma]$ are determined, (1) and (2) can then be used to calculate the inner layer permittivity and conductivity. This step is the "testing phase".

B. Inhomogeneous Inner Layer

For inhomogeneous media, such as the human body, pixel-by-pixel imaging is needed. To do so, the imaging domain is divided into K cylindrical segments ("pixels"), as depicted in Fig. 2c. As a proof of concept, in this work, we chose K=16. Specifically, we chose a uniform square grid where each square is typically 7.5cm×7.5cm in size. As a result, pixels deep into the cylinder are 7.5cm×7.5cm and the ones adjacent to the circular boundary are adjusted accordingly. As seen in Fig. 2c, the outer pixels are modified in size by the enclosing cylinder of radius r_2=15 cm. We remark that when we mention the permittivity or conductivity of a pixel, this refers to the average value across that pixel.

Following the approach in [8]-[10], expressions (3) and (4) are generalized to predict and represent the permittivity and conductivity at each pixel for k=1, 2, …, K. We have,

$$[\varepsilon_r]_{K\times N} = [w_\varepsilon]_{K\times M}[E]_{M\times N} \quad (5)$$
$$[\sigma]_{K\times N} = [w_\sigma]_{K\times M}[E]_{M\times N} \quad (6)$$

We again mention here that M refers to the number of observation points around the cylinder. As part of the "training phase," (5) and (6) must now be enforced for N known values of pixel permittivities and conductivities at their respective locations. In doing so, the matrix entries for $[w_\varepsilon]_{K\times M}$ and $[w_\sigma]_{K\times M}$ are then calculated, using the least square method. To generate the "training" matrix system, the followings have to be varied: a) electrical properties and thickness of the outer layer, b) thickness of the inner layer, and c) electrical properties subject to a given value of ε_r and σ at the k-th pixel. This approach results in an extremely high number of possible tissue variations. Therefore, to reduce the training equations, we introduced some *a priori* information. This *a priori* information includes the a) torso circumference, and b) average permittivity and conductivity of the imaging domain. The latter can be extracted using the process described in [8]-[10].

III. ACCURACY EVALUATION FOR HOMOGENEOUS INNER LAYER

For simplicity, the analysis in this Section assumes a uniform imaging domain, as shown in Fig. 2b. Specifically, the inner layer is assumed to represent the lung tissue as depicted in Table I. A similar analysis was recently carried out in [10], demonstrating that the sensor's accuracy in estimating ε_{r2} can be better than 3%. However, the aforementioned analysis in [10] considered a non-realistic, semi-infinite planar model of the human torso. Here, we consider the sensor's performance for a more realistic scenario, viz. a cylindrical model of the human torso as in Fig. 2b.

A. Modeling

Scattering by the cylindrical human torso shown in Fig. 2b is formulated as a line source scattering from a 2-layer cylinder. The line source is placed on the cylinder's surface and radiates a monotonic field at 40 MHz. We assume this source field to be TM polarized. The details of the radiated and scattered fields are provided in Appendix A.

TABLE II
IMAGING ACCURACY OF THE SENSOR FOR AN INHOMOGENEOUS EXAMPLE

Pixel #	Relative permittivity ε_r			Conductivity σ		
	Actual	Estimated	Error (%)	Actual	Estimated	Error (%)
1	63.5	64.75	1.96	0.38	0.373	-1.8
2	63.5	64.59	1.71	0.38	0.381	0.26
3	63.5	62.67	-1.3	0.38	0.375	-1.31
4	63.5	63.76	0.42	0.38	0.376	-1.05
5	63.5	65.32	2.87	0.38	0.386	1.57
6	68.6	66.8	-2.71	0.42	0.40	-4.98
7	69.22	66.7	-3.63	0.42	0.401	-4.52
8	63.5	64.86	2.14	0.38	0.376	-1.05
9	63.5	62.93	-0.89	0.38	0.375	-1.31
10	67.31	66.65	-0.98	0.42	0.402	-4.28
11	68.58	67.18	-2.03	0.42	0.405	-3.57
12	63.5	64.88	2.17	0.38	0.38	0
13	63.5	64.02	0.84	0.38	0.375	-1.31
14	69.85	69.56	-0.41	0.38	0.387	1.84
15	63.5	65.28	2.81	0.38	0.388	2.10
16	63.5	65.82	3.66	0.38	0.375	-1.31

B. Results

As part of the "training phase," we employed N = 1 to 640 combinations of outer tissue layers in (3) and (4) to calculate $[w_\varepsilon]$ and $[w_\sigma]$. A "testing phase" was then conducted for 400 random test cases. The goal of the "testing phase" was to calculate the error range expected from (5) and (6). For each test case, the absolute percentage errors in estimating the inner layer permittivity, ε_{r2} and conductivity, σ_2 were calculated from:

$$e_\varepsilon = \frac{|\varepsilon_{r,estimated} - \varepsilon_{r,actual}|}{\varepsilon_{r,actual}} \times 100\% \quad (7)$$

$$e_\sigma = \frac{|\sigma_{estimated} - \sigma_{actual}|}{\sigma_{actual}} \times 100\% \quad (8)$$

Here, the subscripts *actual* and *estimated* imply the actual and estimated permittivity and conductivity values, respectively.

Numerical results showed that the error for extracting $\varepsilon_r$was < 5% when: 1) the number of outer tissue layer combinations used to "train" (3) and (4) was $N \geq 300$, 2) the number of sensor observation points was $M \geq 24$, and 3) the sensor length was ≥ 40 cm. Concurrently, the error in extracting σ_2 was < 1%. To our knowledge, this is the highest accuracy reported for body-worn approaches for imaging high-contrast tissues deep into the body.

IV. ACCURACY EVALUATION FOR INHOMOGENEOUS INNER LAYER

A. Modeling

Based on the design guidelines derived in Section III, we consider a sensor that is wrapped around a cylindrical model of the torso having radius 18 cm, shown in Fig. 2a. ANSYS HFSS was used in the simulations, and the simulation set-up is shown in Fig. 2a. The sensor consists of M = 24 probes. We also used N = 400 different combinations of tissues during the "training phase" to determine the weight coefficients $[w_\varepsilon]_{K\times M}$ and $[w_\sigma]_{K\times M}$. The sensor probes were dipoles, 5.3 cm long, viz. λ/141.5 at 40 MHz, where λ=7.5m is the free-space wavelength. That is, we chose a realistic example of the torso. Also, all dipoles were matched to 50Ω.

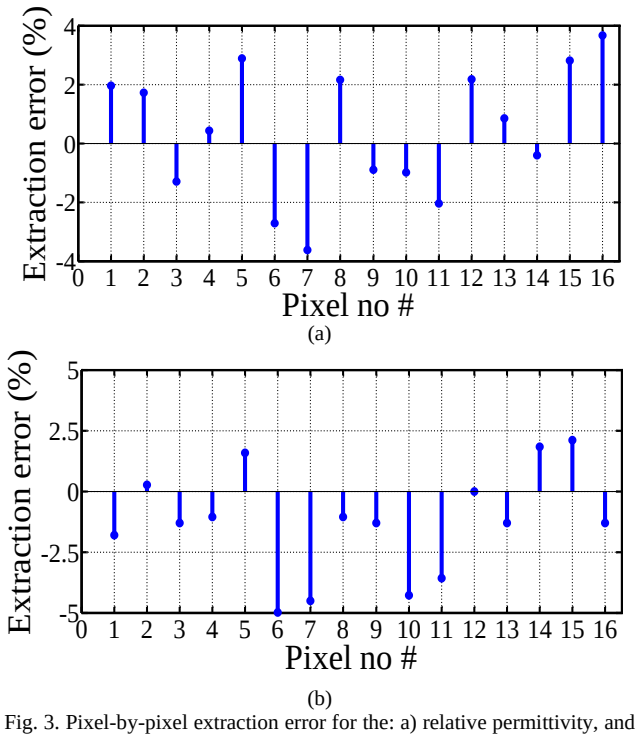

Fig. 3. Pixel-by-pixel extraction error for the: a) relative permittivity, and b) conductivity.

B. Numerical Results

Incorporating the *a priori* information, a) torso circumference, and b) average permittivity and conductivity of the imaging domain, during the "training phase", the tissue electrical properties and thicknesses were varied by ±10% around their nominal values. For the outer layer, these nominal values are given in Table I. For the inner layer, a total of 16 pixels were used to model the inhomogeneous region using values in the range $58.5 < \varepsilon_r < 71.5$ and $0.34 \text{ S/m} < \sigma < 0.42$ S/m.

The "testing phase" was conducted using 400 random test cases. For each test case, the absolute percentage errors in estimating the permittivity and conductivity of each pixel were calculated according to (7) and (8). We found that the percentage errors for each pixel, averaged over the 400 test cases were always < 6%.

To further assess our wrap-around sensor, we proceeded to demonstrate its pixel-by-pixel accuracy for a specific scenario. Specifically, we considered a case that emulates the electrical cross-section of a lung subjected to pulmonary edema. The extracted relative permittivity and conductivity of the cross-section (see Fig. 2d) is given in Table II for 16 pixels. The associated errors calculated using (7) and (8) are further plotted in Fig. 3. We observe that both the permittivity and conductivity were recovered with an error < 5%.

V. Conclusion

An accuracy evaluation was carried out for a wrap-around imaging sensor. The sensor consists of several probes, one transmitting and the others receiving. Imaging of deep human tissues is achieved by using the fields collected at the receiving probes. Specifically, these fields are weighted to determine the permittivity and conductivity at different locations within the enclosed cylindrical structure.

For the first time, this paper provided a validation of the imaging accuracy for this simple, wearable, but also very practical imaging sensor of the torso or other body cross-section. The accuracy of the sensor was evaluated for homogeneous and inhomogeneous cylinder cross-sections. It was shown that the error in determining the cross-section permittivity and conductivity at each pixel was no more than 6%.

Future work will include experimental verification of the proposed imaging method, and further improvement of the sensor's imaging resolution.

Appendix A

The training of the homogeneous cylinder was done using analytical formulas to calculate the surface electric fields. These fields are then used to determine the weight coefficients of (3) and (4) by satisfying (1) for several cases. The excitation was assumed to be a line source, and the radiated fields were found via the addition theorem and by enforcing continuity conditions.

Specifically, given the incident/excitation field [18]-[19],

$$\begin{aligned}\boldsymbol{E_i} &= \hat{\boldsymbol{z}}\frac{-k_0^2 I}{4\omega\epsilon_0}H_0^{(2)}(k_0|\boldsymbol{\rho}-\boldsymbol{\rho}'|)\\ &= \hat{\boldsymbol{z}}\frac{-k_0^2 I}{4\omega\epsilon_0}\sum_{n=-\infty}^{\infty}J_n(k_0\rho)H_0^{(2)}(k_0\rho')e^{jn(\varphi-\varphi')},\ \rho\le\rho'\end{aligned} \tag{A.1}$$

The scattered field in the air medium is [18]-[19],

$$\boldsymbol{E_s} = \hat{\boldsymbol{z}}\frac{-k_0^2 I}{4\omega\epsilon}\sum_{n=-\infty}^{\infty}C_n H_0^{(2)}(k_0\rho)e^{jn\varphi},\ \rho\ge a_1 \tag{A.2}$$

The resulting fields (scattered+incident) in the outer and inner layer, respectively, of Fig. 2b are given by [18]-[19],

$$\boldsymbol{E}_1 = \hat{\boldsymbol{z}}\frac{-k_1^2 I}{4\omega\epsilon_1}\sum_{n=-\infty}^{\infty}\left(a_{n1}J_n(k_1\rho) + b_{n1}Y_n(k_1\rho)e^{jn\varphi},\right. \quad r_2\le\rho\le r_1 \tag{A.3}$$

$$\boldsymbol{E}_2 = \hat{\boldsymbol{z}}\frac{-k_2^2 I}{4\omega\epsilon_2}\sum_{n=-\infty}^{\infty}\left(a_{n2}J_n(k_2\rho) + b_{n2}Y_n(k_2\rho)e^{jn\varphi},\right. \quad \rho\le r_2 \tag{A.4}$$

In (A.1)-(A.4), k_0 is the free-space wavenumber, $k_{1,2}$ is the wavenumber in the outer and inner cylinder layers, ω is the angular frequency, ε_0 is the free-space permittivity, $\varepsilon_{1,2}$ is the permittivity of the outer and inner cylinder layers, I refers to the line source current strength, $r_{1,2}$ is the radius of the outer and inner cylinder layers, $H_0^{(2)}$ is the Hankel function of the second kind of order zero, and J_n and Y_n are the Bessel functions of the first and second kind, respectively, of order *n*. The coefficients a_{n1}, b_{n1}, a_{n2}, b_{n2}, and c_n are obtained by enforcing continuity of the electric and magnetic fields at the cylindrical layer interfaces. They are given by:

$$a_{n1} = \frac{N_1}{D},\ a_{n2} = \frac{\frac{k_1^2}{\varepsilon_1}(XX_1a_{n1} + YY_1b_{n1})}{\frac{k_2^2}{\varepsilon_2}ZZ_1} \tag{A.5}$$

$b_{n1} = \frac{N_2}{D}$, $b_{n2} = 0$ (as the function, Y_n is singular at the center) (A.6)

$$c_n = \frac{X_1a_{n1}+Y_1b_{n1}-Z_1}{K}, \tag{A.7}$$

where

$$N_1 = \begin{vmatrix} LZ_1 - KZ_2 & LY_1 - KY_2 \\ 0 & YY_1ZZ_2 - YY_2ZZ_1 \end{vmatrix} \tag{A.8}$$

$$N_2 = \begin{vmatrix} LX_1 - KX_2 & LZ_1 - KZ_2 \\ XX_1ZZ_2 - XX_2ZZ_1 & 0 \end{vmatrix} \tag{A.9}$$

$$D = \begin{vmatrix} LX_1 - KX_2 & LY_1 - KY_2 \\ XX_1ZZ_2 - XX_2ZZ_1 & YY_1ZZ_2 - YY_2ZZ_1 \end{vmatrix} \tag{A.10}$$

Here, $|\cdot|$ denotes determinant of the matrix. Also:

$$\begin{aligned}
&K = \tfrac{k_0^2}{\varepsilon_0}H_0^{(2)}(k_0a_1),\ L = \tfrac{k_0^2}{\varepsilon_0\eta_0}H_0^{(2)\prime}(k_0a_1),\\
&X_1 = \tfrac{k_1^2}{\varepsilon_1}J_n(k_1a_1),\ X_2 = \tfrac{k_1^2}{\varepsilon_1\eta_1}J_n{}'(k_1a_1),\\
&Y_1 = \tfrac{k_1^2}{\varepsilon_1}Y_n(k_1a_1),\ Y_2 = \tfrac{k_1^2}{\varepsilon_1\eta_1}Y_n{}'(k_1a_1),\\
&Z_1 = \tfrac{k_0^2}{\varepsilon_0}J_n(k_0a_1)H_0^{(2)}(k_0\rho')e^{jn\varphi'},\\
&Z_2 = \tfrac{k_0^2}{\varepsilon_0\eta_0}J_n{}'(k_0a_1)H_0^{(2)}(k_0\rho')e^{jn\varphi'},\\
&XX_1 = J_n(k_1a_2),\ XX_2 = \tfrac{1}{\eta_1}J_n{}'(k_1a_2),\\
&YY_1 = Y_n(k_1a_2),\ YY_2 = \tfrac{1}{\eta_1}Y_n{}'(k_1a_2),\\
&ZZ_1 = J_n(k_2a_2),\ ZZ_2 = \tfrac{1}{\eta_2}J_n{}'(k_2a_2).
\end{aligned} \tag{A.11}$$

VI. References

[1] L. Curiel, R. Chopra and K. Hynynen, "Progress in Multimodality Imaging: Truly Simultaneous Ultrasound and Magnetic Resonance Imaging," *IEEE Trans. Med. Imag.*, vol. 26, no. 12, pp. 1740-1746, Dec. 2007.

[2] J.P. Green, "Bayesian reconstructions from emission tomography data using a modified EM algorithm," *IEEE Trans. Med. Imag.*, vol. 9, no. 1, pp. 84-93, Mar. 1990..

[3] G. Pratx, C.M. Carpenter, C. Sun, and L. Xing, "X-Ray luminescence computed tomography via selective excitation: a feasibility study," *IEEE Trans. Med. Imag.*, vol. 29, no. 12, pp. 1992-1999, Dec. 2010.
[4] P.M. Edic, J. Saulnier, J.C. Newell, and D. Isaacson, "A real-time electrical impedance tomography," *IEEE Trans. Biomed. Eng.*, vol. 42, no. 9, pp. 849-859, Nov. 1995.
[5] R. Paradiso, G. Loriga, and N. Taccini, "A wearable health care system based on knitted integrated sensors," *IEEE Trans. Inf. Technol. Biomed.*, vol. 9, no. 3, Sept. 2005.
[6] A. Bonfiglio and D. De Rossi, Eds., *Wearable Monitoring Systems*, Springer, New York, NY, USA, 2011.
[7] T. Yilmaz and Y. Hao, "Compact resonators for permittivity reconstruction of biological tissues", in *Proc. URSI General Assembly and Scientific Symposium*, pp. 1-4, Aug. 2011.
[8] S. Salman, D.Psychoudakis, and J. L. Volakis, "Determining the relative permittivity of deep embedded biological tissues," *IEEE Antennas Wireless Propag. Lett.*, vol. 11, pp. 1694-1697, 2012.
[9] S. Salman, Z. Wang, E. Colebeck, A. Kiourti, E. Topsakal, and J.L. Volakis, "Pulmonary edema monitoring sensor with integrated body-area network for remote medical sensing," *IEEE Trans. Antennas Propag.*, vol. 62, no. 5, pp. 2787-2794, Feb. 2014.
[10] A. Michel, K. Karathanasis, P. Nepa, and J.L. Volakis, "Accuracy of a conformal sensor for estimating deep tissues dielectric constants," *IEEE Sensors Journal*, 2015.
[11] S. Salman, L. Z. Lee, and J. L. Volakis, "A Wearable Wrap-Around Sensor for Monitoring Deep Tissue Electric Properties", *IEEE Sensor Journal*, Vol. 14, No. 8, Aug 2014
[12] E.C. Fear, S.C. Hagness, P.M. Meaney, M. Okoniewski, and M.A. Stuchly, "Enhancing breast tumor detection with near-field imaging," *IEEE Microw. Mag.*, vol. 3, no. 1, pp. 48-56, Mar. 2002.
[13] J. D. Shea, B.D. Van Veen, and S.C. Hagness, "A TSVD analysis of microwave inverse scattering for breast imaging," *IEEE Trans. Biomed. Eng.*, vol. 59, no. 4, pp. 936–945, Nov. 2011.
[14] S. Gabriel, R. W. Lau, and C. Gabriel, "The dielectric properties of biological tissues—Part II: Measurement in the frequency range 10 Hz to 20 GHz," *Phys. Med. Biol.*, vol. 41, pp. 2251–2269, 1996.
[15] S. Gabriel, R. W. Lau, and C. Gabriel, "The dielectric properties of biological tissues: III. Parametric models for the dielectric spectrum of tissues," *Phys. Med. Biol.*, vol. 41, pp. 2271–2293, 1996.
[16] IEEE Standard for Safety Levels With Respect to Human Exposure to Radiofrequency Electromagnetic Fields, 3 kHz to 300 GHz, IEEE Standard C95.1, 1999.
[17] Evaluating Compliance with FCC Guidelines for Human Exposure to Radio Frequency Electromagnetic Fields, FCC OET Bulletin.65, Washington D.C., Aug. 1997.
[18] C. Balanis, "Advanced electromagnetic engineering," 2nd Edition, *Wiley*, Jan. 2012.
[19] R. F. Harrington, "Time-harmonic electromagnetic fields," *Wiley-IEEE press*, Sep. 2001.

Md Asiful Islam received the B.Sc. and M.Sc. degrees in Electrical and Electronic Engineering both from Bangladesh University of Engineering and Technology, Dhaka, Bangladesh in 2009 and 2013, respectively. He is currently working toward the Ph.D. degree in Electrical and Computer Engineering with the Electroscience Laboratory, The Ohio State University, Columbus, Ohio, USA.

His research interests include medical sensing, machine learning and optimization algorithms in electromagnetics, inverse problems in electromagnetics, bioelectromagnetics and antennas for sensing applications.

Asimina Kiourti (S'10–M'14) received the Diploma in Electrical and Computer Engineering from the University of Patras, Patras, Greece, in 2008, the M.Sc. degree in Technologies for Broadband Communications from University College London, London, U.K., in 2009, and the Ph.D. degree in Electrical and Computer Engineering from the National Technical University of Athens, Athens, Greece, in 2013.

She is currently a Senior Research Associate with the ElectroScience Laboratory, The Ohio State University, Columbus, OH, USA. She has authored or co-authored 23 journal papers, more than 40 conference papers, and 6 book chapters. Her research interests include medical sensing, antennas for medical applications, RF circuits, bioelectromagnetics, and flexible textile and polymer-based electronics.

Dr. Kiourti has been the recipient of more than 40 awards and scholarships, including the IEEE Engineering in Medicine and Biology Society (EMB-S) Young Investigator Award for 2014, the IEEE Microwave Theory and Techniques Society (MTT-S) Graduate Fellowship for Medical Applications for 2012, and the IEEE Antennas and Propagation Society (AP-S) Doctoral Research Award for 2011.

John L. Volakis (S'77–M'82–SM'89–F96) was born in Chios, Greece, on May 13, 1956. He received the B.E. degree (summa cum laude) from Youngstown State University, Youngstown, OH, USA, and the M.Sc. and Ph.D. degrees from The Ohio State University, Columbus, OH, USA, in 1979 and 1982, respectively.

He started his career at Rockwell International (1982–1984), now Boeing Phantom Works. In 1984, he was appointed an Assistant Professor with the University of Michigan, Ann Arbor, MI, USA, becoming a Full Professor in 1994. He also served as the Director of the Radiation Laboratory from 1998 to 2000. Since January 2003, he has been the Roy and Lois Chope Chair Professor of Engineering at The Ohio State University, Columbus, OH, USA, and also serves as the Director of the ElectroScience Laboratory. He has carried out research on antennas, medical sensing, computational methods, electromagnetic compatibility and interference, propagation, design optimization, RF materials and metamaterials, RFIDs, milli-meter waves and terahertz, body-worn wireless technologies, and multiphysics engineering. His publications include eight books, including Approximate Boundary Conditions in Electromagnetics (IET, 1995), Finite Element Methods for Electromagnetics (Wiley-IEEE Press, 1998) Antenna Engineering Handbook (McGraw-Hill, 2007, 4th ed.), Small Antennas (McGraw-Hill, 2010), and Integral Equation Methods for Electromagnetics (SciTech, 2011)]. His papers include over 350 journal papers, more than 650 conference papers, and 25 book chapters. He has also written several well-edited course packs and has delivered

short courses on antennas, numerical methods, and frequency-selective surfaces.

Dr. Volakis is a Fellow of the Applied Computational Electromagnetics Society and a member of the URSI Commissions B and E, and currently serves as the Chair of USNC/URSI Commission B. He was the recipient of the University of Michigan (UM) College of Engineering Research Excellence Award in 1998, and in 2001 he received the UM, Department of Electrical Engineering and Computer Science Service Excellence Award. In 2010 he received the Ohio State University Clara and Peter Scott award for outstanding academic achievement. Also, in 2014 he received the IEEE Antennas and Propagation Society (AP-S) Distiguished Achievement Award and the IEEE AP-S C-T Tai Educator Award. He was listed (2004) by ISI among the top 250 most referenced authors. His mentorship includes over 80 doctoral students/post-doctorals with 30 of them receiving Best Paper awards at international conferences. He was the 2004 President of the IEEE AP-S and served on the AdCom of the IEEE AP-S from 1995 to 1998. He also served as an associate editor for the IEEE TRANSACTIONS ON ANTENNAS AND PROPAGATION from 1988 to 1992, Radio Science from 1994 to 1997, the IEEE Antennas and Propagation Society Magazine (1992–2006), Journal of Electromagnetic Waves and Applications, and URSI Bulletin. Further, he served on the IEEE wide and AP-S Fellows evaluation committee. In 1993 he chaired the IEEE AP-S Symposium and Radio Science Meeting in Ann Arbor, MI, USA, and cochaired the same symposium in 2003 at Columbus, OH, USA.